ISSN 0036-0236, Russian Journal of Inorganic Chemistry, 2016, Vol. 61, No. 11, pp. 1347–1360. © Pleiades Publishing, Ltd., 2016.
Original Russian Text © E.P. Simonenko, N.P. Simonenko, G.P. Kopitsa, V. Pipich, V.G. Sevastyanov, N.T. Kuznetsov, 2016, published in Zhurnal Neorganicheskoi Khimii, 2016, Vol. 61, No. 11, pp. 1399–1413.

SYNTHESIS AND PROPERTIES OF INORGANIC COMPOUNDS

How Xerogel Carbonization Conditions Affect the Reactivity of Highly Disperse SiO_2–C Composites in the Sol–Gel Synthesis of Nanocrystalline Silicon Carbide

E. P. Simonenko[a, *], N. P. Simonenko[a], G. P. Kopitsa[b, c], V. Pipich[d], V. G. Sevastyanov[a], and N. T. Kuznetsov[a]

[a] *Kurnakov Institute of General and Inorganic Chemistry, Russian Academy of Sciences, Leninskii pr. 31, Moscow, 119991 Russia*

[b] *St. Petersburg Institute of Nuclear Physics, St. Petersburg, Russia*

[c] *Grebenshchikov Institute of Silicate Chemistry, Russian Academy of Sciences, St. Petersburg, Russia*

[d] *JCNS, Forschungszentrum Juelich GmbH, Outstation at MLZ, Garching, Germany*

**e-mail: ep_simonenko@mail.ru*

Received May 23, 2016

Abstract—A transparent silicon polymer gel was prepared by sol–gel technology to serve as the base in the preparation of highly disperse SiO_2–C composites at various temperatures (400, 600, 800, and 1000°C) and various exposure times (1, 3, and 6 h) via pyrolysis under a dynamic vacuum (at residual pressures of ~1×10^{-1} to 1×10^{-2} mmHg). These composites were X-ray amorphous; their thermal behavior in flowing air in the range 20–1200°C was studied. The encapsulation of nascent carbon, which kept it from oxidizing in air and reduced the reactivity of the system in SiC synthesis, was enhanced as the carbonization temperature and exposure time increased. How xerogel carbonization conditions affect the micro- and mesostructure of the xerogel was studied by ultra-small-angle neutron scattering (USANS). Both the carbonization temperature and the exposure time were found to considerably influence structure formation in highly disperse SiO_2–C composites. Dynamic DSC/DTA/TG experiments in an inert gas flow showed that the increasing xerogel pyrolysis temperatures significantly reduced silicon carbide yields upon subsequent heating of SiO_2–C systems to 1500°C, from 35–39 (400°C) to 10–21% (1000°C).

DOI: 10.1134/S0036023616110206

Methods for preparing highly disperse SiO_2–C composites are well documented, as they are widely used in various fields of science and engineering. The most common applications of these systems are as fillers for lithium ion batteries [1–13], inert or electrically conductive catalyst supports, active ingredients of electrochemical sensors [14–26], and precursor systems in the synthesis of silicon carbide and silicon nitride materials [27–41].

Li et al. [1] described the mutual synergistic effect on the electrochemical characteristics of a mesoporous material based on SiO_2 nanospheres coated with a thin carbon layer, and showed the promise of this material for use in lithium ion batteries. Yuan et al. [2] deposited carbon on SiO_2 nanospheres, which were prepared by hydrolyzing tetraethoxysilane (TEOS) with water in ethanol catalyzed by $NH_3 \cdot H_2O$, by reacting cetyl triammonium bromide, ammonium persulfate, and aniline on their surfaces in an acidified aqueous–alcoholic medium (10 M HCl), followed by centrifugation and carbonization at 750°C for 2 h in vacuo. Dirican et al. [3, 4] prepared a $Si/SiO_2/C$ flexible nanofiber anode material by electrospinning (at 60°C) of a silicon slurry in a DMF solution of TEOS and polyacrylonitrile with additions of hydrochloric acid (37%) with subsequent curing at 280°C and carbonization at 700°C (2 h) under an argon atmosphere. The thus-fabricated fibers were additionally coated with a thin amorphous carbon film by CVD with acetylene as the precursor. For manufacturing a SiO_2/C nanostructured fibrous composite by electrospinning, Wu et al. [5] introduced SiO_2 (30 ± 5 nm) nanoparticles into a DMF solution of polyacrylonitrile. The $Li_3V_2(PO_4)_3/(SiO_2 + C)$ composite described by Lai et al. [6] was fabricated using a silicon-and-carbon-containing precursor, namely dihydroxydiphenylsilane. Tao et al.'s study [7] was directed to the manufacture and characterization of $Si@SiO_2@C$ double-walled nanocomposites, where silicon nanoparticles were first oxidized at 700°C in air to generate a SiO_2 shell and then coated with an epoxy resin layer followed by drying and carbonization. Hassan et al. [8] reported their method for preparing

$Si/SiO_2/C$ materials using rapid heating. A positive effect caused by the use of mechanochemical treatment in addition to sol–gel technology for preparing SiO_2/C nanocomposites is described [9, 10]. To manufacture SiO_2/C nanocomposites Gong et al. [11] coated SiO_2 nanospheres (prepared by sol–gel technology) with aniline followed by diazotization reaction, drying, and carbonization under an argon atmosphere. Kim et al. [12] fabricated porous SiO_2/C microparticles by hydrolyzing TEOS in the presence of a triblock copolymer on polystyrene templates; they studied the roles of sucrose and boric acid additives. One-dimensional hierarchic structures $SiC@SiO_2@C$ were prepared by chemical vapor deposition [13]. A two-stage hydrothermal and heat treatment was used to prepare $SiO_2@C@$graphene candidate materials for lithium ion batteries [14].

Zhong et al. [14] prepared SiO_2–C mesoporous composites, which were functionalized by SO_3H groups due to active carbon, as a candidate acid catalyst for the dimerization of styrene and α-methylstyrene by hydrolyzing TEOS in the presence of sucrose and triblock copolymer, followed by drying and carbonization (N_2, 700°C). These composites showed themselves as very promising supports for metal catalysts, e.g., platinum [15, 24] and ruthenium [16], for use in organic [15] and inorganic [16] heterogeneous catalytic syntheses. The immobilization of various metal phthalocyanines on highly disperse and electrically conductive SiO_2–C composites prepared primarily by sol–gel technology, makes possible the design of electrochemical sensors for, e.g., 4-aminophenol [17], nitrites in meat products and water [18], oxygen dissolved in water [19], ascorbic acid and dopamine [20], etc. Canevari et al. [21] deposited Nb_2O_5 thin films on ultrafine SiO_2–C powders by sol–gel technology in the spin-coating variant to fabricate an electrode for the simultaneous determination of hydroquinone and pyrocatechol. A carbon-coated silica immobilization matrix was used for the electrochemiluminescence detection of tumor markers [25]. The conversion of rice husk (with additional carbon) produces formulations that which show promise for bioimaging or drug delivery [22]. Ebrahim et al. [23] described the preparation of candidate silica gel based sorbents and consider their NO_2 sorption capacities. Katok et al. [26] developed a method to produce a material efficient for the sorption of mercury cations from aqueous solutions.

The characteristics of silica–carbon precursor systems are also of great importance for the preparation of silicon carbide, especially in highly disperse state. In spite of the great diversity of SiO_2 reduction methods (magnesiothermy [27, 28], alumotherny [29], combustion reactions [30], electrospinning from salt melts [31], with silicon additions [32], or carbothermy [33–42]), it is clear that the method used to prepare SiO_2–C precursor composites and the chemical nature, purity, degree of homogenization, dispersion, component ratio, and component reactivities, determine both the synthesis parameters and properties of SiC.

Sol–gel technology has great merits in the context of preparing highly disperse, chemically reactive MO_x-C composites with the distributions of amorphous oxides and carbon in each other as uniform as possible, which was shown earlier (by us, too) for the preparation of nanocrystalline carbides (SiC, TiC, ZrC, TaC, HfC, Ta_4ZrC_5, and Ta_4HfC_5) under relatively soft conditions, i.e., at 1500°C or lower temperatures [41–47]. It was noticed that the reactivities of the systems prepared by sol–gel technology are affected not only by the ratio of the components (metal oxides and carbon) produced by pyrolyzing xerogels, but also by the pyrolysis process parameters, namely temperature and exposure time. Earlier experiments to prepare nanosized silicon carbide powders [41] and to fill-in porous composites by a SiC matrices [42] showed that the highly disperse SiO_2–C precursor systems produced by the carbonization of silicon polymer xerogels in an inert medium or under a reduced pressure at various temperatures (at 825 ± 25 and 600 ± 10°C, respectively), have strongly differing parameters. For the composite prepared at higher temperature, the encapsulation of nascent carbon by amorphous silica is distinct; specific surface areas differ considerably. The carbonization temperature commonly used for phenol formaldehyde resins (~800–1000°C) is the temperature at which the ultimate destruction of the polymer occurs, including the dehydrogenation of aromatic rings [48–50]. The process is carried out under a coke coverage under atmospheric pressure. However, when the carbonization of phenol formaldehyde resins (which perform as the carbon source during controlled TEOS hydrolysis in their solutions [41, 42]) is carried out under dynamic vacuum conditions, there is probability that the pyrolysis process parameters would change; that is, one can affect the reactivity of a SiO_2–C composite in the subsequent carbothermic SiC synthesis via changing the temperature and time of xerogel carbonization under dynamic vacuum conditions.

Our goal in this study was to elucidate how the parameters (temperature and exposure time) of carbonization of the silicon polymer xerogels prepared by sol–gel technology influence the reactivity of thus-produced highly disperse SiO_2–C precursor systems for subsequent preparation of nanosized silicon carbide.

EXPERIMENTAL

The chemicals used were tetraethoxysilane $Si(OC_2H_5)_4$ (specialty grade 14-5; TEOS), bakelite varnish LBS-1, formic acid CH_2O_2 (pure for analysis

grade), and acetone CH_3COCH_3 (pure for analysis grade).

X-ray powder diffraction patterns were measured on a Bruker D8 Advance diffractometer (CuK_α radiation, 0.02° resolution, accumulation time per point: 0.3 s).

IR transmission spectra of samples were recorded on an InfraLum FT-08 FTIR spectrometer as Nujol mulls between KBr glasses.

The thermal behavior of powders in air was studied using an SDT Q-600 simultaneous TG/DTA/TG analyzer (heating rate: 20 K/min; air or argon flow rate: 100 mL/min).

Scanning electron microscopy (SEM) experiments were performed on an NVision 40 (Carl Zeiss) three-beam workstation; elemental microanalysis was performed with an EDX Oxford Instruments energy dispersive analysis unit.

Ultra-small-angle neutron scattering (USANS) was measured on a KWS-3 instrument (relocated at the FRM-II reactor in Garching, Germany), which is a high-resolution small-angle diffractometer equipped with a double-focusing toroidal mirror that provides for the high resolution in transmitted pulses of up to 1×10^{-4} Å^{-1} [51, 52]. The measurement neutron wavelength was $\lambda = 12.8$ Å ($\Delta\lambda/\lambda = 0.2$). The use of two sample–detector distances ($S_D = 1$ and 10 m) provided for neutron scattering intensity measurements in the range $2.5 \times 10^{-4} < q < 1.4 \times 10^{-2}$ Å^{-1}. Scattered neutrons were detected by a 2D position-sensitive scintillation ^{6}Li detector (active spot was $\varnothing = 8.7$ cm with a spatial resolution of 0.36 × 0.39 mm).

Samples of highly disperse SiO_2–C systems were mounted between two silica glasses (KWS-3). The initial spectra for each q range were corrected for scattering from the instrument hardware, cell (silica glasses), and ambient background using a standard procedure [53]. The thus-measured isotropic 2D spectra were azimuthally averaged and reduced to absolute magnitudes by norming to the incoherent scattering cross-section of PlexiGlass with account to the detector efficiency [53] and the bulk density ρ_h for each sample. All measurements were performed at room temperature. The primary data processing was with the QtiKWS program [54].

Thus, USANS gave us the complete scattering pattern for SiO_2–C samples for transmitted pulses in the range $2.5 \times 10^{-4} < q < 1.5 \times 10^{-2}$ Å^{-1}, which corresponds to structural analysis in the range of characteristic sizes R_c from ≈20 nm to ≈1.4 μm.

RESULTS AND DISCUSSION

Transparent silicon polymer gels were prepared by hydrolyzing TEOS with water in the presence of a polymeric carbon source, which was a phenol formaldehyde resin. Since earlier [40] we showed that carbon taken in an excess amount over stoichiometry (1) made it possible to reduce the probability of occurrence of SiO-yielding side reactions and avoid decreasing the yield of the desired product (SiC), in this study the ratio $n(C) : n(SiO_2)$ was 3.05.

$$SiO_2(s) + 3C(s) = SiC(s) + 2CO(g). \quad (1)$$

During hydrolysis followed by gel formation, the ratio $n(H_2O) : n\{Si(OC_2H_5)_4\}$ was five and the ratio $n(CH_2O_2) : n\{Si(OC_2H_5)_4\}$ was four; the temperature was in the range 40–50°C. The resulting gel was stepwise dried at 70–150°C until the weight change stopped.

For pyrolyzing organic components, the xerogel was heat-treated under a dynamic vacuum (the residual pressure was ~1×10^{-1} to 1×10^{-2} mmHg) at 400, 600, 800, and 1000°C with exposure at the highest temperature for 1, 3, and 6 h (Table 1). The highly disperse SiO_2–C systems obtained at a carbonization temperature of 400°C, were brownish (which might signify an incomplete pyrolysis of the phenol formaldehyde resin); the systems obtained at higher temperatures (600, 800, or 1000°C) were black powders.

The primary distinction of the IR spectrum (Fig. 1) of the sample prepared under the mildest conditions (400°C, 1 h) from the spectrum of the sample prepared under the most severe conditions (1000°C, 6 h) consists of additional absorption bands associated with adsorbate and chemically bound water. There are a rather strong absorption band ν(OH) in the range 3260–3700 cm^{-1}, an absorption band of adsorbate water δ(H_2O) in the range 1570–1690 cm^{-1} (which can overlap the overtone absorption bands of the $(SiO_4)_n$ framework), and an absorption band peaking at 975 cm^{-1} with a shoulder at 880–890 cm^{-1}, associated with the stretching and bending vibrations of Si–(OH). Those additional bands disappear only in the samples prepared at carbonization temperatures of 800 and 1000°C. The low-intensity absorption band peaking at 1513 cm^{-1} (which disappears from the IR spectra of products only when the xerogel pyrolysis temperature is 600°C or higher), may be assigned to remnant aromatic moieties of the xerogel.

In all samples, the IR spectra feature a strong and broadened absorption band peaking at 1035–1075 cm^{-1} (ν(Si–(OSi)); the shift of the peak of this band toward lower wavenumbers as the xerogel carbonization temperature increases can signify the formation of a more ordered three-dimensional framework Si–O–Si. The shoulder peaking at 1205–1215 cm^{-1} can indicate the presence of bulk species on the surface where the angles between SiO_4 tetrahedra approach 180°, and the low-intensity shoulder at ~1150 cm^{-1} can belong to the C–O bond in the Si–O–C structure.

X-ray powder diffraction showed that all SiO_2–C systems obtained upon the carbonization of xerogels were X-ray amorphous (Fig. 2). When the heat treat-

Table 1. Peak temperatures of thermal events observed in SiO_2–C systems prepared under various conditions (an air flow; 100–1200°C)

Sample code	SiO_2–C carbonization parameters		Weight loss end temperature, °C	Peak temperature of exotherm, °C (with weight loss)		Peak temperature of exotherm, °C (without weight loss)	
	temperature, °C	exposure time, h					
400_1	400	1	~700	607	711*	–	1173
400_3		3	~700	601	716*	–	–
400_6		6	~700	608	711*	–	–
600_1	600	1	~716	604	707*	–	–
600_3		3	~740	623	725*	–	–
600_6		6	~763	628	732, shoulder	–	–
800_1	800	1	~855	660	751	–	–
800_3		3	~835	654	742	–	1129
800_6		6	~877	678	766	–	1150
1000_1	1000	1	~953	678	775	–	1103
1000_3		3	~945	680	778	1072	1146
1000_6		6	~990	669	778	1082	1140

* A very weak shoulder.

ment temperature was 600°C or higher, however, a second, far less intense diffuse halo, signifying local ordering in the material, appeared in X-ray diffraction patterns in the range $2\theta = 41°–48°$ (peaking at ~44°).

From the earlier results [41, 42], we suspect that, at higher xerogel carbonization temperatures, the vitrification of nascent SiO_2 can occur and, as a result, encapsulation of pyrolytic carbon, which should give rise to a reduced reactivity of the system. This is manifested in the alteration of the thermal behavior of the system in flowing air (Fig. 3, Table 1).

Therefore, for SiO_2–C samples produced by carbonization at 400°C, regardless of the exposure time, there is virtually no obstacles to carbon burning-out:

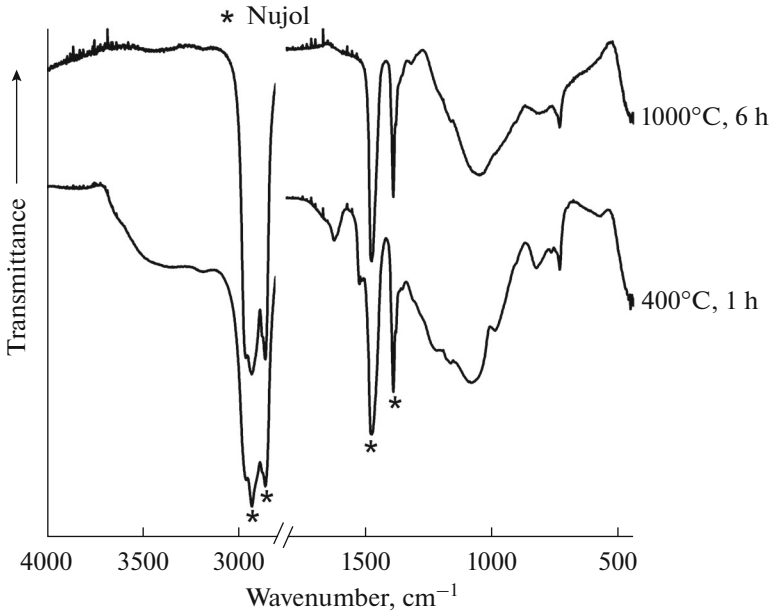

Fig. 1. IR spectra of highly disperse SiO_2–C samples prepared by sol–gel technology at xerogel carbonization temperatures of (lower panel) 400 (1 h) and (upper panel) 1000°C (6 h).

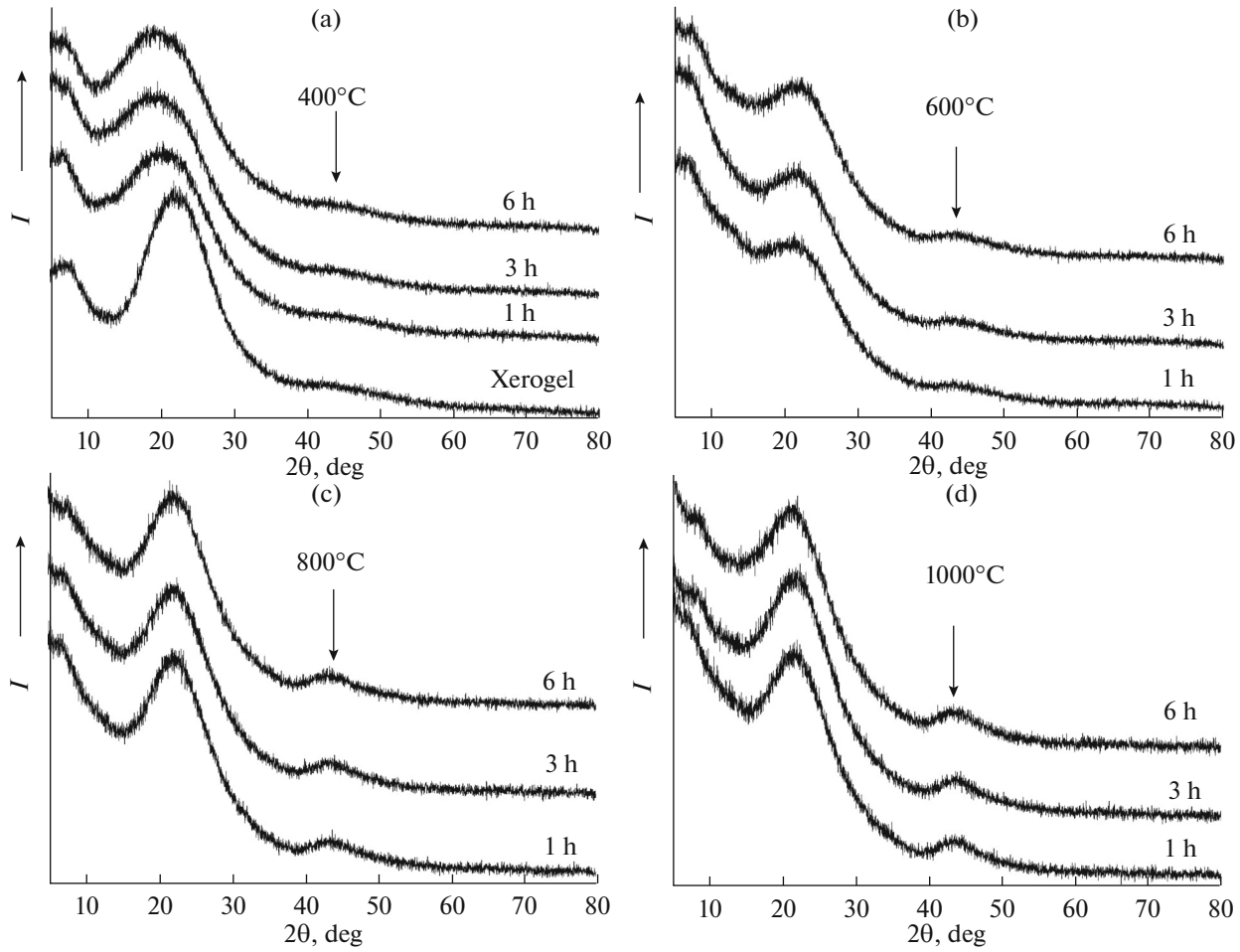

Fig. 2. X-ray diffraction patterns of SiO_2–C samples prepared at various xerogel carbonization temperatures: (a) 400, (b) 600, (c) 800, and (d) 1000°C.

the process starts at ~400°C and ends at ~700°C. As early as for 600°C carbonization there is observed a considerable broadening of the exotherm associated with the oxidation of carbon in the SiO_2–C composite; as the exposure time increases (1 → 6 h), the peak of the exotherm shifts from 604 to 628°C and a shoulder appears on the high-temperature side. The weight loss end temperature also increases appreciably (from 716 to 763°C).

For the samples prepared from xerogels carbonized at 800 and 1000°C, carbon burning-out is a two-step process, with two peaks in the exotherms. While the samples prepared at 800°C show an increase in oxidation temperature in response to increasing exposure time, for the composites prepared at 1000°C this trend is less distinct: there are virtually no shifts in the peaks of thermal events, but the weight loss end temperature increases noticeably (to ~990°C).

In general, the ever strengthening effects that hinder carbon oxidation in the SiO_2–C system are observed as the carbonization temperature goes from 600 to 800°C and higher; the effect caused by temperature is more significant than the effect caused by changing exposure time.

For some samples (mostly for those prepared at 800 and 1000°C), DSC curves feature weak and diffuse exotherms with peaks at 1100–1173°C, which are not accompanied by weight change and are likely to arise from the structuring of an amorphous phase. For the samples that were formed at 1000°C and longer exposure times (3 and 6 h), in addition, there is a thermal event with a peak at 1072–1082°C, which can be assigned to SiO_2 crystallization.

X-ray powder diffraction and IR spectroscopy showed that, as a result of heating of SiO_2–C composites prepared under various conditions, to 1200°C in flowing air under thermoanalytical conditions, a cristobalite phase was formed only in the samples that experienced the most severe carbonization (Fig. 4; samples 1000_3 and 1000_6).

One can see in Fig. 4 that an absorption band peaking at 620 cm^{-1} appears in the IR spectra for the cristobalite phase, and the 800-cm^{-1} absorption band nar-

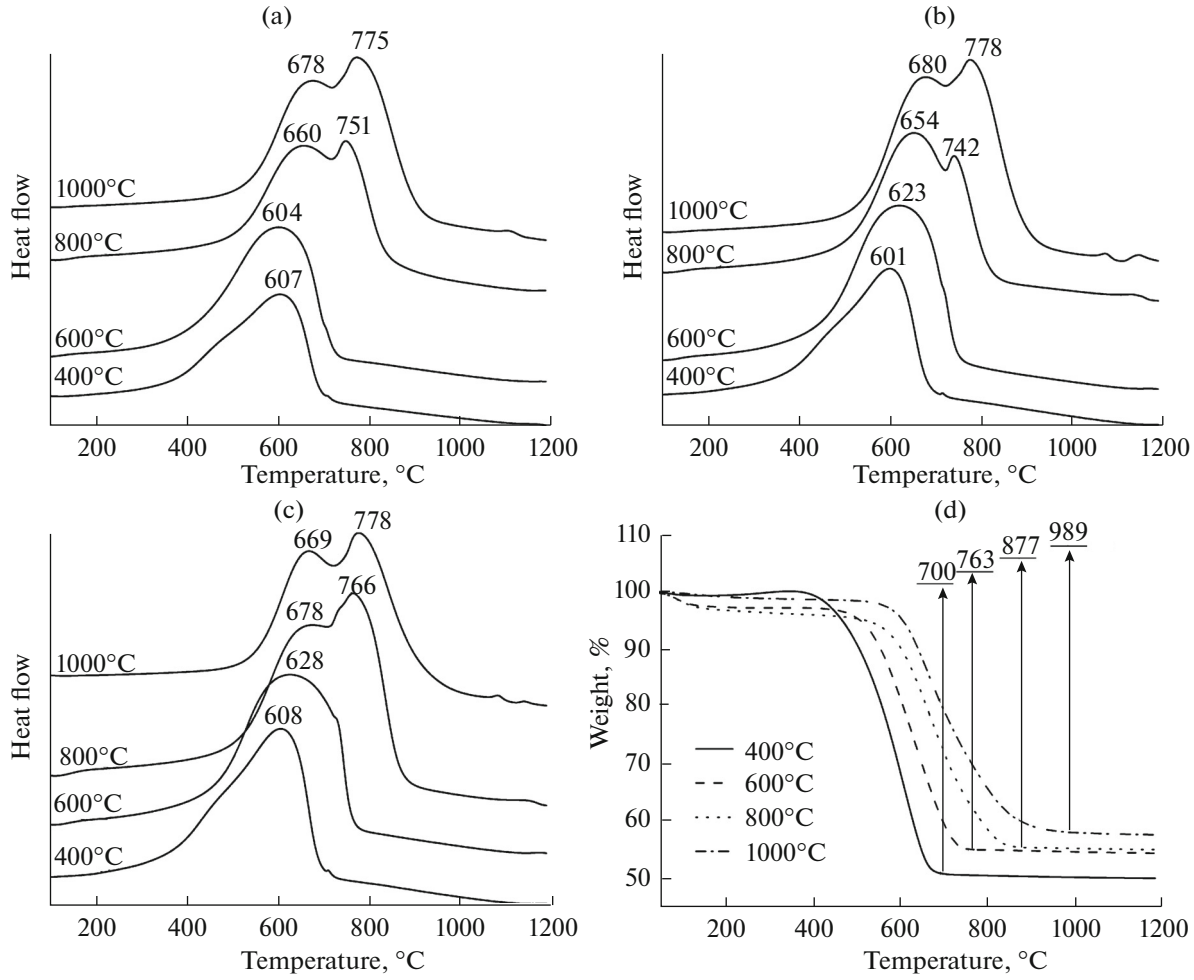

Fig. 3. Thermal behavior in flowing air: (a–c) DSC curves for SiO_2–C samples prepared at exposure time of 1 (a), 3 (b), and (c) 6 h; and (d) TG curves for systems prepared at various temperatures with 6-h exposure.

rows and gains in intensity. These data support our suspicion that the broad low-intensity exotherm peaking at 1072–1082°C that appears on DSC curves for the samples prepared at 1000°C (3 and 6 h) and does not appear in the other samples (Fig. 3, Table 1), is due to the formation of cristobalite phase.

The SEM images taken after carbon was removed upon heating to 1200°C in flowing air also show considerable differentiation of the processes (Fig. 5). For the SiO_2 powder that remained after carbon was burnt out from samples 400_1–400_6, there is observed increased porosity, there are no signatures of incipient melting, the particle shapes of the precursor xerogel remain almost unchanged, and particle sizes in SiO_2 agglomerates are 20–50 nm. For the SiO_2 powers based on the precursor systems prepared at 600°C, macroparticles also retain their shapes, but micromorphology has clear traces of particle coarsening and growing together to larger and surface-melted species. For the SiO_2 grains prepared by carbon burning-out from systems 800_1–800_6, which in general retained the xerogel geometry, we failed to detect nanoparticles: a glassy surface was observed. The same is observed for the sample obtained from system SiO_2–C 1000_1. For longer exposures (3 and 6 h), xerogel carbonization at 1000°C appreciably alters not only the micromorphology, but also the macromorphology of the powder; the powder is hollow spherulitic granules having walls 5–10 μm thick, with cristobalite crystallization lines on the surfaces. Obviously, blowing-up of the precursor xerogel macroparticles resulted from the oxidation of carbon residing in the less accessible closed pores.

In order to elucidate the specifics of micro- and mesostructure of highly disperse SiO_2–C systems and how the carbonization temperature and exposure time affect their structuring character, we used USANS.

Figure 6 shows log–log plots of $d\Sigma(q)/d\Omega$, measured differential macroscopic cross-sections of USANS from SiO_2–C samples prepared by heat treatment with 1-h exposures at 400, 600, 800, and 1000°C, respectively. The SiO_2–C samples prepared with 6-h

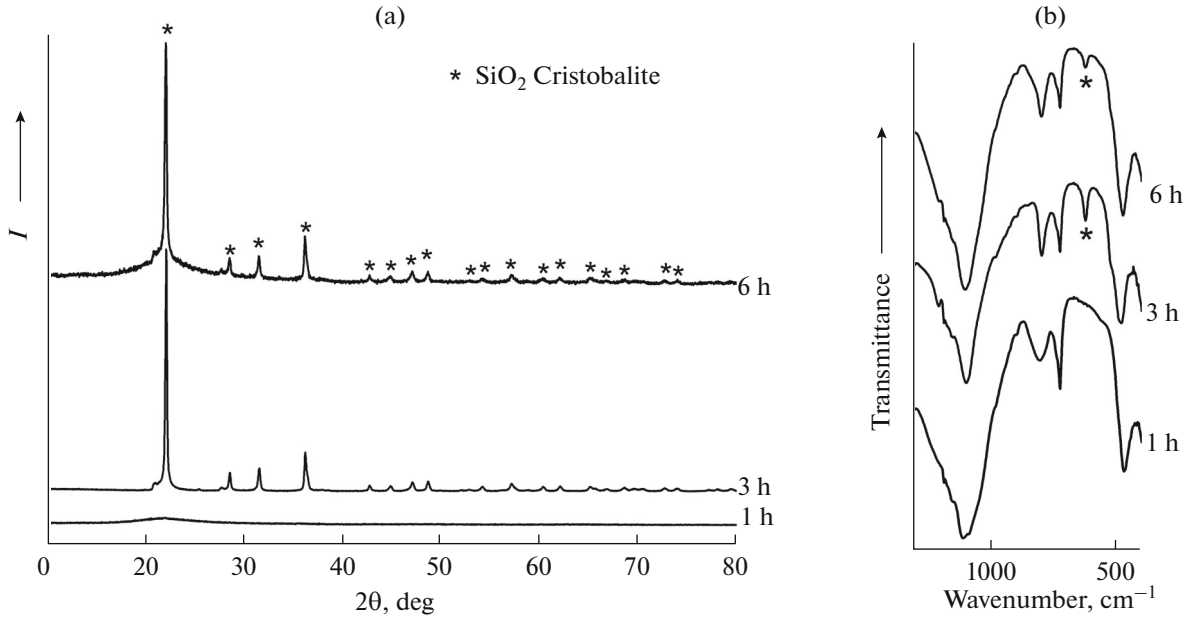

Fig. 4. (a) X-ray diffraction patterns and (b) IR spectra of SiO_2 samples prepared by heating to 1200°C in flowing air in DSC/DTA/TG, of the SiO_2–C precursor systems prepared at a carbonization temperature of 1000°C.

exposures have a similar scattering pattern. Since for better perception the values of $d\Sigma(q)/d\Omega$ for samples 600_1, 800_1, and 1000_1 in Fig. 6 are multiplied by a factor of 5, 10, and 15, respectively, we should mention that, actually, the true USANS magnitude of $d\Sigma(q)/d\Omega$ increases as either the heating temperature or the exposure time increases, and this is a clear indication that heat treatment reduced the nuclear density homogeneity of these samples over the scale of radii from 20 nm to ≈1.4 μm.

A common feature for all SiO_2–C tested samples is the free q ranges on the relevant curves where the USANS cross-section $d\Sigma(q)/d\Omega$ behaves fundamentally differently. Over the range $7 \times 10^{-4} < q < 7 \times 10^{-3}$ Å^{-1}, the scattering cross-section $d\Sigma(q)/d\Omega$ obeys the power law q^{-n}. The values of n found from the slope of the straight sections of experimental $d\Sigma(q)/d\Omega$ curves are in the range 3.79–3.94 (Table 2), which corresponds to scattering on items that have fractal surface dimensions $2.06 < (D_s = 6 - n) < 2.21$ [55].

Deviations from the q^{-n} power law in the behavior of scattering cross-section $d\Sigma(q)/d\Omega$ are observed in the ranges of small and large transmitted pulses q for all samples. At small q ($<7 \times 10^{-4}$ Å^{-1}), the deviations are due to the entrance to the Guinier mode, where the scattering is determined by the characteristic size R_c of independently scattering large-scale inhomogeneities (aggregates). From an analysis of Guinier scattering, by the slopes of $d\Sigma(q)/d\Omega$ versus q^2 curves one can estimate the radius of gyration R_g of the inhomogeneities and, accordingly, their characteristic size R_c, for example (in the case of spheres) through the relationship $R_c = \sqrt{5/3}R_g$ [56]. In the range of large transmitted pulses, the $d\Sigma(q)/d\Omega$ cross-section is no longer dependent on q (becomes constant) and is likely due to incoherent scattering from water molecules sorbed from air and scattering from inhomogeneities of the order of the neutron wavelength used in the given experiment.

Thus, the pattern observed in Fig. 6 is a typical pattern scattering for structurally disordered systems, e.g., for a porous (solid–pore) structure with a fractal interface [55]. From the foregoing, we fitted the scattering from SiO_2–C samples over the entire range of the study by the unified exponential power expression below, which was advanced for one-level structures [57]:

$$\frac{d\Sigma(q)}{d\Omega} = G\exp\left(-\frac{q^2R_g^2}{3}\right) + \frac{B}{\hat{q}^n} + I_{inc}. \qquad (2)$$

Here, $\hat{q} = q/[\mathrm{erf}(qR_g/6^{1/2})]^3$ is transmitted pulse q normed to the error function erf(x).

This procedure makes it possible to correctly describe the behavior of the scattering cross-section $d\Sigma(q)/d\Omega$ in an "intermediate" range between $qR_c < 1$ (the Guinier approximation) and $qR_c \gg 1$ (q^{-n} asymptotics), where the contributors to scattering are both inhomogeneities having characteristic scale of R_c, and their local structures [57]. The parameter I_{inc}, which is a q-independent constant, is due to incoherent scattering. The G and B amplitudes are the Guinier and power frequency factors, respectively, the first being

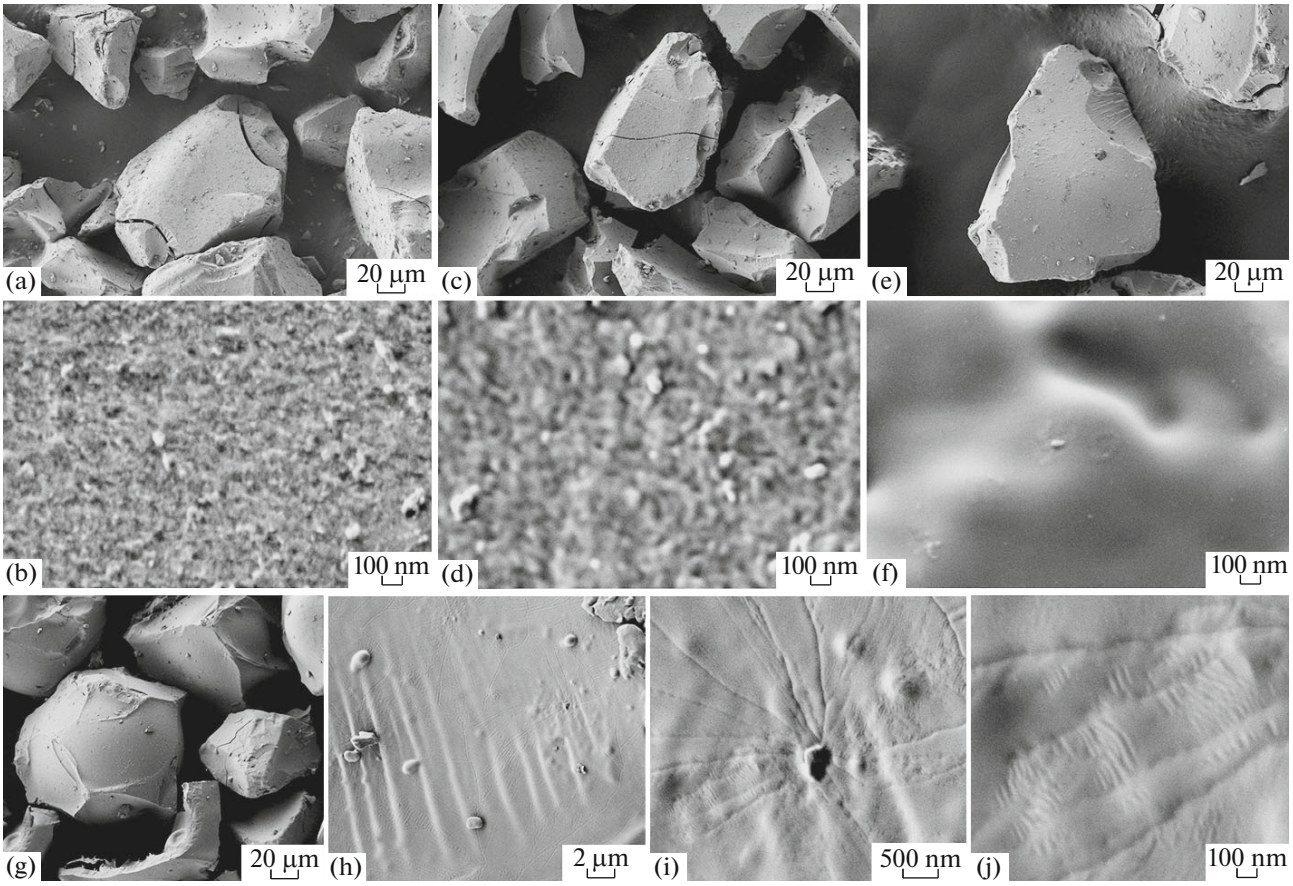

Fig. 5. Micrographs of SiO_2 powders prepared by heating, in flowing air, of SiO_2–C systems where xerogel carbonization occurred at (a, b) 400, (c, d) 600, (e, f) 800, and (g–j) 1000°C for 6 h.

directly proportional to the product of the number of inhomogeneities in the scattering volume and ρ, the average neutron scattering amplitude density on them [56], and the second being dependent on local structure characteristics, in the case at hand, on D_S, the surface dimension of scattering inhomogeneities [55]:

$$B(D_S) = \pi\rho^2\rho_0\Gamma(5 - D_S) \times \sin\left[(D_S - 1)(\pi/2)\right] N_0. \quad (3)$$

Here, Γ is gamma function, ρ_0 is density of the solid, and ρ for a molecule containing more than one element is determined as

Table 2. Micro- and mesostructure parameters of SiO_2–C samples derived from USANS data

Sample	Structure parameters				
	$G \times 10^7$, $cm^2\ g^{-1}$	R_c, Å	$B \times 10^{-7}$, $cm^2\ g^{-1}\ Å^{-n}$	$D_S = 6 - n$	S_0, $m^2\ g^{-1}$
400_1	5.63 ± 0.07	8588 ± 172	4.8 ± 0.2	2.06 ± 0.03	1.69 ± 0.11
400_6	6.13 ± 0.03	8230 ± 165	6.5 ± 0.3	2.10 ± 0.03	1.92 ± 0.14
600_1	6.26 ± 0.07	8192 ± 151	6.4 ± 0.5	2.06 ± 0.03	2.00 ± 0.12
600_6	6.45 ± 0.05	7759 ± 155	11.9 ± 0.5	2.11 ± 0.03	2.36 ± 0.15
800_1	6.76 ± 0.07	8100 ± 162	7.8 ± 0.2	2.17 ± 0.03	2.47 ± 0.12
800_6	6.95 ± 0.07	7546 ± 151	14.7 ± 1.5	2.21 ± 0.03	3.16 ± 0.15
1000_1	7.01 ± 0.07	7746 ± 155	8.5 ± 0.2	2.15 ± 0.03	4.51 ± 0.20
1000_6	7.19 ± 0.04	7051 ± 141	19.1 ± 0.9	2.17 ± 0.03	5.23 ± 0.23

$$\rho = \sum_i b_i N_i \frac{\rho_0 N_A}{M}. \quad (4)$$

Here, N_A is Avogadro's number, M is molar weight, b_i is scattering length from element i in the molecule, and N_i is number of atoms of the element. The constant N_0 is related to the specific surface area of the surface fractal as $S_0 = N_0 r^{2-D_S}$, where r^{2-D_S}, and determined by the measurement scale. For smooth surfaces, $D_S = 2$ and $N_0 = S_0$.

To obtain ultimate results, expression (2) was convoluted with the resolution function of the instrument. Experimental differential cross-section $d\Sigma(q)/d\Omega$ plots were processed by the least squares over the entire range of study. The results are shown in Fig. 6 and in Table 2.

An analysis of the structural parameters (Table 2), which directly determine the observed USANS character, shows a distinct dependence of the structure of SiO_2–C test samples on the carbonization conditions of the precursor xerogels. One can clearly see that an increase either in the heat-treatment temperature or in the exposure time of xerogels at the highest temperature gives rise to a noticeable (up to 15% upon 6-h exposure at 1000°C) decrease in the size R_c of their constituent large-scale aggregates; simultaneously, their surface fractal dimension D_S increases to give rise, in turn, to an appreciable (almost 2.5-fold) rise in their specific surface areas S_0, determined by coarse particles (with diameters ranging from 40 nm to 2.8 μm). The observed structural alterations are likely to arise from the greater depth of pyrolysis of the carbon source (phenol formaldehyde resin) and, accordingly, the appearance of more cavities on aggregate surfaces.

Comparative reactivities of SiO_2–C composites prepared under various conditions were ascertained via studying their thermal behaviors in flowing argon in the range 20–1500°C (Figs. 7, 8). In Fig. 7, which shows full patterns of DSC/DTA/TG experiments in flowing argon for composites prepared under the mildest (400°C, 1 h) and the most severe carbonization conditions (1000°C, 6 h), one can see, for all samples, a characteristic weight loss of ~2–4% at temperatures below 300°C accompanied with an endotherm related to the desorption of volatile gases. In addition, the samples prepared by pyrolyzing xerogels at 400°C and, less distinct, those at 600°C, show a considerable weight loss (11 and 3–4.5%, respectively) in the range 300–800°C. We assign this feature to the pyrolysis of organic moieties that survive low-temperature carbonization (destruction of aromatic rings) in the products.

Since earlier thermodynamic simulations [40, 58] showed that SiC cannot be prepared carbothermically at temperatures below 800°C even at pressures reduced to 1×10^{-3} atm, in order to cancel out the effects of attendant desorption and destruction of aromatic moieties, we performed the quantitative analysis

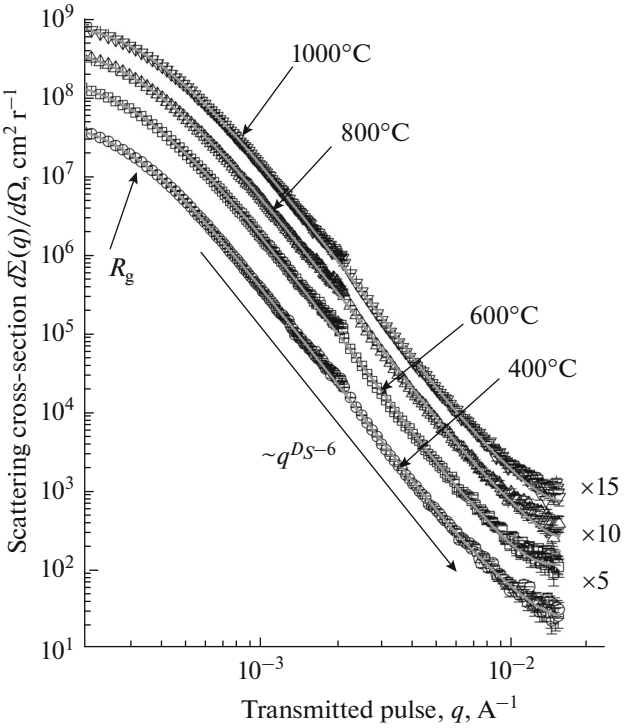

Fig. 6. USANS differential cross-section $d\Sigma(q)/d\Omega$ versus pulse q transmitted by SiO_2–C samples prepared upon heat treatment with 1-h exposure at 400, 600, 800, and 1000°C. For better perception, the $d\Sigma(q)/d\Omega$ values for samples 600_1, 800_1, and 1000_1 are multiplied by 5, 10, and 15, respectively.

of weight loss due to silicon carbide formation in the range 800–1500°C (Table 3).

A rise in xerogel carbonization temperature is seen to considerably reduce the reactivities of the resulting SiO_2–C systems: SiC yield decreases from ~35–39 to 10–20% (especially for samples 800_6 and 1000_1–1000_6). Some reduction in chemical reactivity also occurs when the exposure time increases; this is especially prominent for samples prepared at 1000°C.

X-ray powder diffraction patterns (Fig. 9) and IR spectra prove that the observed weight loss is due to silicon carbide formation during dynamic DSC/TG experiments; as one can judge from broadened reflections, cubic or hexagonal SiC is formed. The silicon carbide reflection intensity varies symbatically to the yield value derived from the weight loss during carbothermic reduction in the range 800–1500°C (Table 3; Figs. 7, 8); the highest yield is observed for the SiO_2–C composite that was carbonized under the mildest conditions. The SiC crystallite size calculated by the Scherrer relationship is 14–18 nm, for sample 1000_6, ~39 nm.

The thermal behavior in flowing air for SiO_2–C–SiC products obtained in the carbothermic synthesis of silicon carbide in a dynamic mode (under

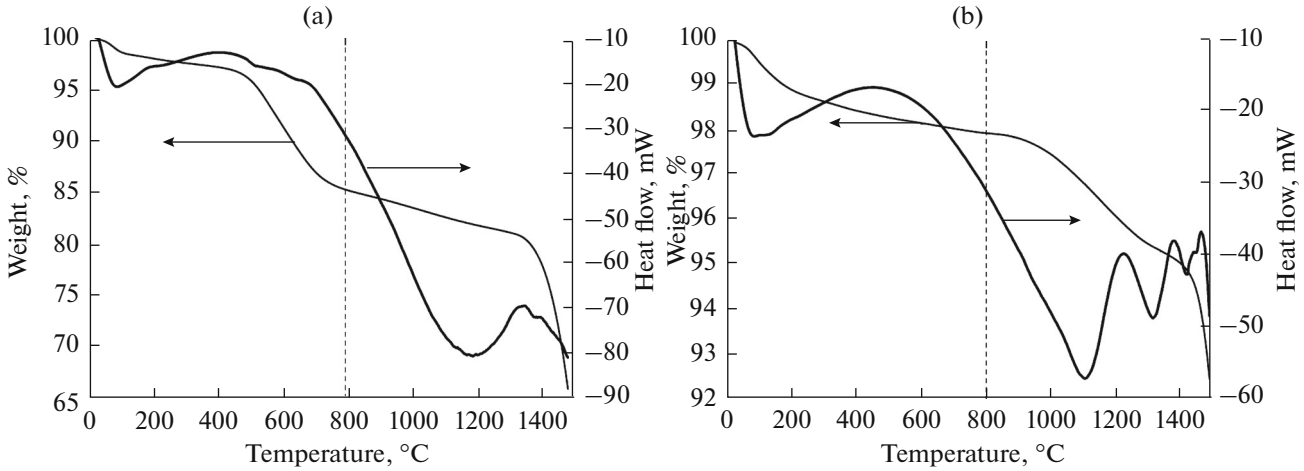

Fig. 7. Thermal behavior in flowing argon of SiO_2–C composite prepared under (a) the mildest (400°C, 1 h) and (b) severe (1000°C, 6 h) carbonization conditions.

DSC/DTA/TG conditions in flowing argon at temperatures up to 1500°C), was studied in the range 20–1400°C. We expected nanocrystalline silicon carbide to oxidize at temperatures starting with 800–1000°C [41] with an attendant weight gain correlating with its percentage and reactivity, which is related to its particle size. In Fig. 10, which exemplifies data for systems exposed for 1 h during xerogel carbonization, for all SiO_2–C–SiC composites (regardless of the conditions under which the SiO_2–C precursors were synthesized), however, we see an appreciable increase in the temperature at which residual carbon burns out due to considerable carbon encapsulation upon additional heating of SiO_2–C powders to 1500°C. For the SiO_2–C–SiC samples produced in flowing argon from composites 400_1–800_3, there is no overlap between the oxidation of encapsulated carbon (which occurs in two steps) and the oxidation of nanosized silicon carbide produced in flowing argon: carbon burn-out ends at 970–1010°C (samples 400_1–600_6) and 1000–1100°C (samples 800_1–800_3), and the weight gain due to SiC oxidation starts at 1020–1060 and 1140–1180°C, respectively. The SiO_2–C–SiC sample prepared from precursor system 800_6 behaves outstandingly: at ~1035°C, it experiences a weight gain due to SiC oxidation, which is then changed by weight loss due to the oxidation of encapsulated carbon continuing up to 1275°C. For the SiO_2–C–SiC systems prepared from SiO_2–C precursor samples 1000_1–1000_6, weight loss involves three steps and continues until 1400°C. Thus, we cannot make a reliable conclusion whether we are dealing with the overlap of the oxidation of SiC and the oxidation of encapsulated carbon, or we observe the encapsulation of the silicon carbide itself which keeps it from reacting with air oxygen.

Table 3. Weight loss from SiO_2–C samples in the range 800–1500°C upon heating to 1500°C in flowing argon

Sample code	Weight loss, %	SiC yield*, %
400_1	22.7	39
400_3	20.5	35
400_6	21.5	37
600_1	18	31
600_3	14.8	25
600_6	17.3	30
800_1	13.6	23
800_3	15	26
800_6	12.2	21
1000_1	11.7	20
1000_3	12.3	21
1000_6	5.6	10

* In the approximation of occurrence of the SiC formation reaction alone with possible SiO distillation ignored.

In general, we can conclude that, the higher is the calculated silicon carbide yield, the higher is the weight gain observed in the analysis of the thermal behavior of SiO_2–C–SiC samples. There is undoubted correlation between the reactivity of the SiO_2–C precursor systems prepared under various conditions, exposure temperature, and exposure time during the carbonization of silicon polymer xerogels.

CONCLUSIONS

Thus, we have prepared a set of SiO_2–C composite samples by the heat treatment, under reduced pressure, of silicon polymer xerogels produced by sol–gel technology, with considerably differing pyrolysis parameters (temperature: 400, 600, 800, and 1000°C; exposure time: 1, 3, and 6 h). All these systems are X-ray amorphous, but as temperature rises, a second diffuse

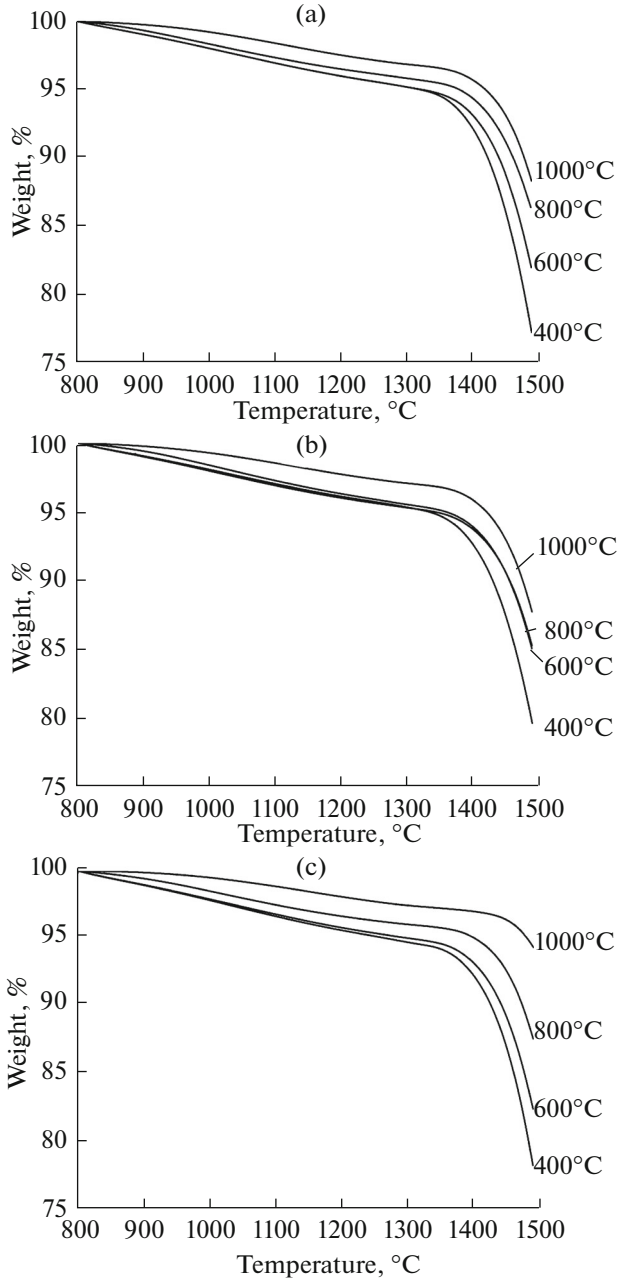

Fig. 8. TG curves in flowing argon in the range 800–1500°C for SiO_2–C systems prepared at various temperatures and with exposure times of (a) 1, (b) 3, and (c) 6 h.

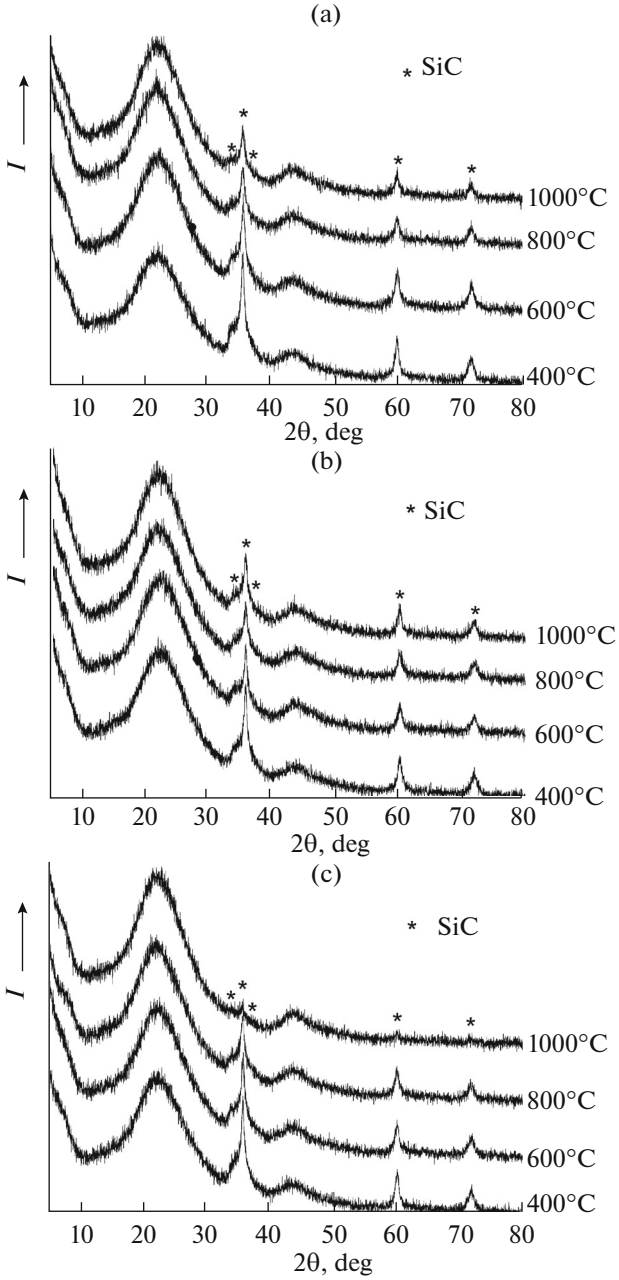

Fig. 9. X-ray diffraction patterns of SiO_2–C–SiC products obtained during the analysis of thermal behavior, in flowing argon in the range of up to 1500°C, of SiO_2–C systems prepared at various exposure temperatures and exposure times of (a) 1, (b) 3, and (c) 6 h.

halo of increasing intensity appears in their X-ray diffraction patterns, indicating local structuring. USANS shows an appreciable influence of the xerogel carbonization conditions on the structuring of products: as the exposure temperature and exposure time increase, the characteristic size of large-scale aggregates (having diameters of from ≈40 nm to ≈2.8 μm) decreases and their fractal surface dimension increases. IR spectra imply that the pyrolysis of organic components (primarily the dehydrogenation of aromatic moieties) occurs incompletely in samples 400_1–400_6, which were prepared at xerogel carbonization temperature of 400°C, and this is confirmed by the thermal analysis of these systems in flowing argon. The analysis of the thermal behavior of the prepared SiO_2–C systems in flowing air shows that carbon burning-out in samples 400_1–400_6 ends at a temperature as low as 700°C; when higher xerogel carbonization temperatures are used (600–1000°C), carbon generated upon pyrolysis

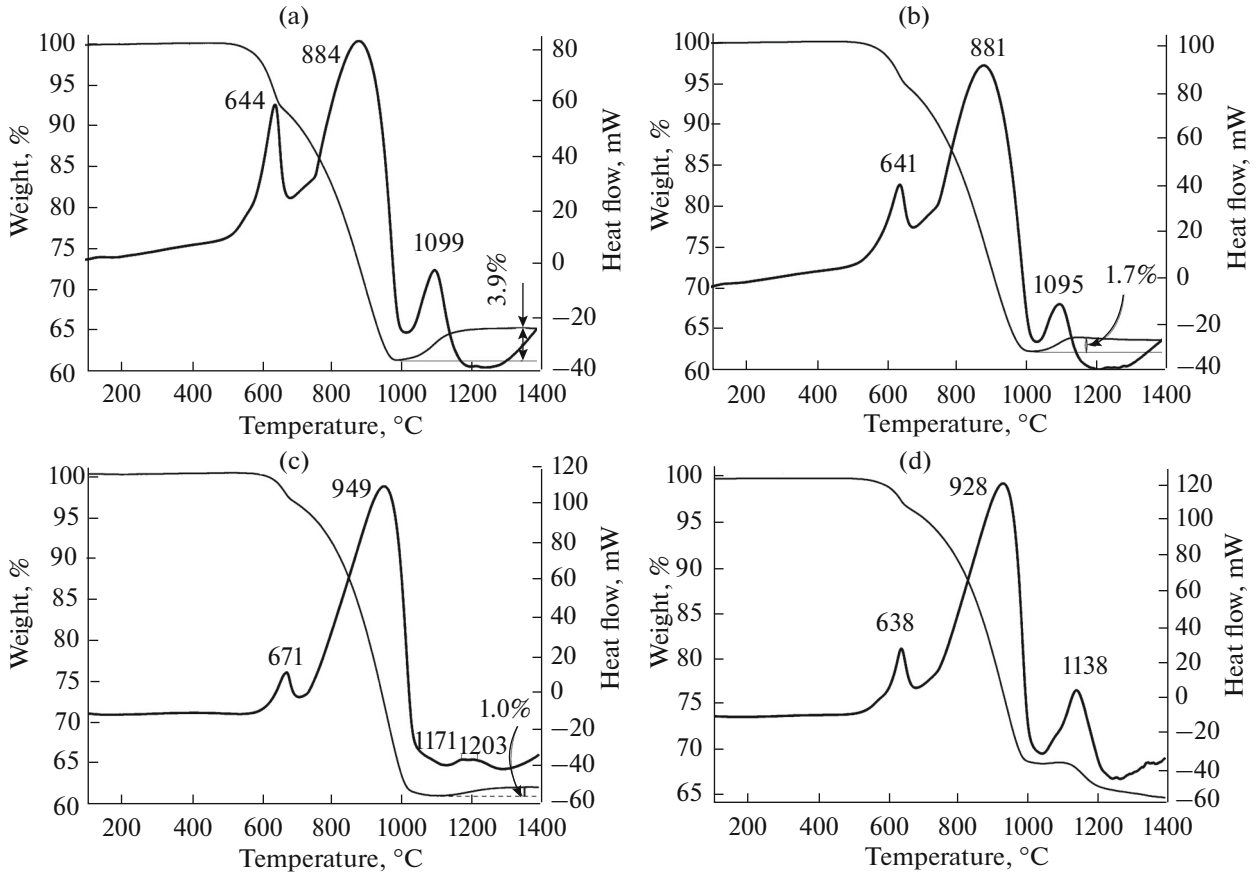

Fig. 10. Thermoanalytical data in flowing air for the SiO_2–C–SiC products obtained during the analysis of the thermal behavior in flowing argon of SiO_2–C systems (Table 3) that were prepared at carbonization temperatures of 400 (a), 600 (b), (c) 800, and C (d) 1000° (exposure time: 1 h).

is encapsulated by the second component (SiO_2). Manifestations of this effect are a considerable increase in the weight loss end temperature (up to ~990°C in sample 1000_6) and the broadening and appearance of a second peak of the carbon oxidation exotherm. One more manifestation is the microstructural alteration of silicon dioxide powers produced by the oxidation of SiO_2–C composites. In samples obtained after heating to 1200°C under DSC/TG conditions in flowing air, the increasing xerogel carbonization temperature gives rise to the coarsening of constituent particles of granules until complete merging and the appearance of a glassy surface; in samples 1000_3 and 1000_6, the shapes of macroparticles change. For the latter, we should mention the formation of a well-crystallized cristobalite phase upon heating in flowing air to 1200°C, which we failed to attain earlier [59] in xerogels prepared by hydrolyzing TEOS (with formic acid as the catalyst) even when we heated them up to 1400°C.

The practicability of modifying the reactivity of SiO_2–C composites prepared by sol–gel technology via modifying xerogel carbonization conditions has been discovered as a result of analyzing the thermal behavior of the systems formed systems during heating up to 1500°C in an inert gas (argon) flow. At temperatures above 800°C, all systems underwent weight loss associated with carbothermal SiC synthesis, which was confirmed by the phase composition of the products as probed by X-ray powder diffraction. As the xerogel carbonization temperature increased from 400 to 1000°C, the calculated silicon carbide yield decreased from 35–39 to 10–21%. An increase in exposure time carbonization temperature to 6 h also considerably reduced SiC percentage in the reaction products.

In general, relying on the data we gained, for the preparation of silicon carbide at the lowest temperatures (which makes it possible to prepare nanosized and weakly aggregated powders), we may recommend to use the SiO_2–C precursor systems prepared at the least temperature carbonization temperature (400°C), despite an incomplete pyrolysis of phenol formaldehyde resins under these conditions. This is due to the following: a rise in carbonization temperature to 600°C, especially in 6 h, leads to a prominent reduction in reactivity, which is manifested as carbon

encapsulation and the associated decrease in silicon carbide yield under the conditions of thermal analysis in flowing argon, from 35–39 to 25–31%. At 400°C, the destruction of the polymeric carbon source to yield large amounts of hazardous gaseous and liquid products (including phenol) are over, and the dehydrogenation of aromatic moieties, which occurs at higher temperatures, does not interfere with SiC synthesis by the carbothermic reaction. Our experiments show that the increasing exposure time during the carbonization of silicon polymer xerogel at 400°C does not appreciably increase the pyrolysis depth of phenol formaldehyde resin. Therefore, the most rational way to obtain a maximally reactive SiO_2–C system that would make it possible to prepare nanosized SiC at lowest temperatures, is to use the mildest carbonization mode: a dynamic vacuum ($\sim 1 \times 10^{-1}$–1×10^{-2} mmHg), temperature of 400°C, and exposure time of 1 h.

ACKNOWLEDGMENTS

This study was supported by grants for young scientists from the President of the Russian Federation (grants MK-1435.2013.3 and MK-4140.2015.3) and by the Russian Foundation for Basic Research (project no. 14-03-31002 mol_a).

REFERENCES

1. H.-H. Li, X.-L. Wu, H.-Z. Sun, et al., J. Phys. Chem. C **119**, 1021 (2015). doi 10.1021/jp511435w
2. Y. Yuan, S. Wang, Z. Kang, et al., Electrochemistry (Tokyo) **83**, 421 (2015). doi 10.5796/electrochemistry.83.421
3. M. Dirican, O. Yildiz, Y. Lu, et al., Electrochim. Acta **169**, 52 (2015). doi 10.1016/j.electacta.2015.04.035
4. M. Dirican, M. Yanilmaz, K. Fu, et al., J. Electrochem. Soc. **161**, A2197 (2014). doi 10.1149/2.0811414jes
5. X. Wu, Z.-Q. Shi, C.-Y. Wang, and J. Jin, J. Electroanal. Chem. **746**, 62 (2015). doi 10.1016/j.jelechem.2015.03.034
6. C. Lai, J. Wei, Z. Wang, et al., Solid State Ionics **272**, 121 (2015). doi 10.1016/j.ssi.2015.01.01
7. H.-C. Tao, X.-L. Yang, L.-L. Zhang, and S.-B. Ni, Ionics **20**, 1547 (2014). doi 10.1007/s11581-014-1138-8
8. F. M. Hassan, V. Chabot, A. R. Elsayed, et al., Nano Lett. **14**, 277 (2014). doi 10.1021/nl403943g
9. A. Molkenova and I. Taniguchi, Adv. Powder Technol. **26**, 377 (2015). doi 10.1016/j.apt.2014.11.013
10. P. Lv, H. Zhao, J. Wang, et al., J. Power Sources **237**, 291 (2013). doi 10.1016/j.jpowsour.2013.03.054
11. H. Gong, N. Li, and Y. Qian, Int. J. Electrochem. Sci. **8**, 9811 (2013).
12. Y.-K. Kim, J.-W. Moon, J.-G. Lee, et al., J. Power Sources **272**, 689 (2014). doi 10.1016/j.jpowsour.2014.08.128
13. M. Zhang, Z. J. Li, J. Zhao, et al., RSC Adv. **4**, 55224 (2014). doi 10.1039/C4RA11931B
14. R. Zhong, L. Peng, F. de Clippel, et al., ChemCatChem **7**, 3047 (2015). doi 10.1002/cctc.201500728
15. C. Fang, Y. Chen, H. Mao, et al., Gaodeng Xuexiao Huaxue Xuebao **36**, 124 (2015). doi 10.7503/cjcu20140753
16. Y. Zhou, G. Lan, B. Zhou, et al., Chin. J. Catal. **34**, 1395 (2013). doi 10.1016/S1872-2067(12)60596-8
17. A. Rahim, N. Muhammad, U. Nishan, et al., RSC Adv. **5**, 87043 (2015). doi 10.1039/C5RA18617J
18. A. Rahim, L. S. S. Santos, S. B. A. Barros, et al., Electroanal. **26**, 541 (2014). doi 10.1002/elan.201300468
19. A. Rahim, L. S. S. Santos, S. B. A. Barros, et al., Sens. Act. B: Chem. **177**, 231 (2013). doi 10.1016/j.snb.2012.10.110
20. S. B. A. Barros, A. Rahim, A. A. Tanaka, et al., Electrochim. Acta **87**, 140 (2013). doi 10.1016/j.electacta.2012.09.012
21. T. C. Canevari, L. T. Arenas, R. Landers, et al., Analyst **138**, 315 (2013).
22. S. Pandey, A. Mewada, M. Thakur, et al., RSC Adv. **4**, 1174 (2014). doi 10.1039/C3RA45227A
23. A. M. Ebrahim, B. Levasseur, and T. J. Bandosz, Langmuir **29**, 6895 (2013). doi 10.1021/la4008137
24. B. Lombardi, F. Pompeo, A. N. Scian, and N. N. Nichio, Mater. Lett. **106**, 393 (2013). doi 10.1016/j.matlet.2013.05.083
25. Y. Zhang, W. Liu, S. Ge, et al., Biosens. Bioelectron. **41**, 684 (2013). doi 10.1016/j.bios.2012.09.044
26. K. V. Katok, R. L. D. Whitby, F. Fayon, et al., ChemPhysChem **14**, 4126 (2013). doi 10.1002/cphc.201300832
27. T.-D. Nguyen, J. A. Kelly, W. Y. Hamad, and M. J. MacLachlan, Adv. Funct. Mater. **25**, 2175 (2015). doi 10.1002/adfm.201404304
28. P. Liu, S. Xie, M. Peng, et al., J. Sol-Gel Sci. Technol. **73**, 270 (2015). doi 10.1007/s10971-014-3576-1
29. M. Karbasi, M. Razavi, M. Azadi, and L. Tayebi, Nano **8**, 1350059/1 (2013). doi 10.1142/S1793292013500598
30. A.-M. Chu, M., M.-L. Qin, B.-R. Jia, et al., Int. J. Min. Met. Mater. **20**, 76 (2013). doi 10.1007/s12613-013-0696-5
31. C.-R. Zhao, J.-Y. Yang, and S.-G. Lu, Wuji Huaxue Xuebao **29**, 2543 (2013). doi 10.3969/j.issn.1001-4861.2013.00.371
32. Y.-C. Jo, M.-R. Youm, S.-I. Yun, et al., J. Kor. Ceram. Soc. **50**, 402 (2013). doi 10.4191/kcers.2013.50.6.402
33. E. P. Simonenko, N. P. Simonenko, M. A. Zharkov, et al., J. Mater. Sci. **50**, 733 (2015). doi 10.1007/s10853-014-8633-1
34. M.-Y. Fan, W.-J. Yun, J. Li, et al. Rengong Jingti Xuebao **42**, 1445 (2013).
35. X. Guo, L. Zhu, W. Li, et al., J. Adv. Ceram. **2**, 128 (2013). doi 10.1007/s40145-013-0050-4
36. M. Fan, W. Yuan, C. Deng, and H. Zhu, Adv. Mater. Res. **634**, 1990 (2013). 10.4028/www.scientific.net/AMR.634-638.1990
37. L. G. Ceballos-Mendivil, R. E. Cabanillas-Lopez, J. C. Tanori-Cordova, et al., Solar En. **116**, 238 (2015). doi 10.1016/j.solener.2015.04.006

38. M.-R. Youm, S.-W. Park, and Y.-W. Kim, J. Kor. Ceram. Soc. **50**, 31 (2013). doi 10.4191/kcers.2013.50.1.31
39. V. V. Chesnokov, V. S. Luchihina, and I. P. Prosvirina, Diam. Relat. Mater. **60**, 14 (2015). doi 10.1016/j.diamond.2015.10.006
40. V. G. Sevastyanov, Y. S. Ezhov, E. P. Simonenko, and N. T. Kuznetsov, Mater. Sci. Forum **457–460**, 59 (2004). doi 10.4028/www.scientific.net/MSF.457-460.59
41. E. P. Simonenko, N. P. Simonenko, A. V. Derbenev, et al., Russ. J. Inorg. Chem. **58**, 1143 (2013). doi 10.1134/S0036023613100215
42. V. G. Sevast'yanov, E. P. Simonenko, N. P. Simonenko, et al., Kompozity Nanostrukt. **6**, 198 (2014).
43. V. G. Sevast'yanov, E. P. Simonenko, N. A. Ignatov, et al., Inorg. Mater. **46**, 495 (2010). doi 10.1134/S0020168510050109
44. V. G. Sevastyanov, E. P. Simonenko, N. A. Ignatov, et al., Russ. J. Inorg. Chem. **56**, 661 (2011). doi 10.1134/S0036023611050214
45. E. P. Simonenko, N. A. Ignatov, N. P. Simonenko et al., Russ. J. Inorg. Chem. **56**, (2011). 1681. doi 10.1134/S0036023611110258
46. E. P. Simonenko, N. P. Simonenko, Yu. S. Ezhov, et al., Yadern. Fiz. Inzh. **5**, 337 (2014). doi 10.1134/S207956291404006X
47. E. P. Simonenko, N. P. Simonenko, Yu. S. Ezhov, et al., Phys. At. Nucl. **78**, 1357 (2015). doi 10.1134/S106377881512011X
48. I. D. Simonov-Emel'yanov and N. L. Shembel', Plast. Massy, No. **9**, 10 (2010).
49. I. D. Simonov-Emel'yanov, N. L. Shembel', and L. A. Kuklina, Konstrukt. Kompozit. Mater., No. 1, 27 (1999).
50. V. V. Korshak, *Chemical Structure and Temperature Characteristics of Polymers* (Nauka, Moscow, 1970) [in Russian].
51. A. Radulescu, E. Kentzinger, J. Stellbrink, et al., Neutron News **16**, 7 (2005).
52. G. Goerigk and Z. Varga, J. Appl. Crystallogr. **44**, 337 (2011).
53. G. D. Wignall and F. S. Bates, J. Appl. Crystallogr. **20**, 28 (1987).
54. http://www.iff.kfa-juelich.de/~pipich/dokuwiki/doku.php/qtikws.
55. H. D. Bale and P. W. Schmidt, Phys. Rev. Lett. **38**, 596 (1984).
56. A. Guinier and G. Fournet, *Small Angle Scattering of X-rays* (Wiley, New York, 1955).
57. G. Beaucage, J. Appl. Crystallogr. **28**, 717 (1995).
58. R. G. Pavelko, V. G. Sevast'yanov, Yu. S. Ezhov, et al., Inorg. Mater. **43**, 700 (2007). doi 10.1134/S0020168507070059
59. E. P. Simonenko, A. V. Derbenev, N. P. Simonenko, et al., Russ. J. Inorg. Chem. **60**, 1444 (2015). doi 10.1134/S0036023615120220

Translated by O. Fedorova